# Independent brain $^{18}$F-FDG PET attenuation correction using a deep learning approach with Generative Adversarial Networks

**Karim Armanious[1,2] MSc,**
**Thomas Küstner [1,2,4] PhD,**
**Matthias Reimold[3] MD,**
**Konstantin Nikolaou[1] MD,**
**Christian La Fougère[3] MD,**
**Bin Yang[2] PhD,**
**Sergios Gatidis[1] MD**

*1. University Hospital Tübingen, Department of Radiology, Diagnostic and Interventional Radiology, Tübingen, Germany*
*2. University of Stuttgart, Institute of Signal Processing and System Theory, Stuttgart, Germany*
*3. University Hospital Tübingen, Department of Radiology, Nuclear Medicine, Tübingen, Germany*
*4. School of Biomedical Engineering & Imaging Sciences, King's College London, St. Thomas' Hospital, London, UK*

*Keywords:* $^{18}$F-FDG-PET
-Attenuation correction
-Deep learning
-Generative Adversarial Networks

***Corresponding author:***
Sergios Gatidis MD,
University Hospital Tübingen
Hoppe-Seyler-Str. 3, 72076
Tübingen, Germany
Tel: +49 7071 29 86676, Fax: +49 7071 29 5845
sergios.gatidis@med.uni-tuebingen.de

*Received:*
2 August 2019
*Accepted:*
30 August 2019

## Abstract

**Objective:** Attenuation correction (AC) of positron emission tomography (PET) data poses a challenge when no transmission data or computed tomography (CT) data are available, e.g. in stand alone PET scanners or PET/magnetic resonance imaging (MRI). In these cases, external imaging data or morphological imaging data are normally used for the generation of attenuation maps. Newly introduced machine learning methods however may allow for direct estimation of attenuation maps from non attenuation-corrected PET data ($PET_{NAC}$). Our purpose was thus to establish and evaluate a method for independent AC of brain fluorine-18-fluorodeoxyglucose ($^{18}$F-FDG) PET images only based on $PET_{NAC}$ using Generative Adversarial Networks (GAN). **Subjects and Methods:** After training of the deep learning GAN framework on a paired training dataset of $PET_{NAC}$ and the corresponding CT images of the head from 50 patients, pseudo-CT images were generated from $PET_{NAC}$ of 40 validation patients, of which 20 were used for technical validation and 20 stemming from patients with CNS disorders were used for clinical validation. Pseudo-CT was used for subsequent AC of these validation data sets resulting in independently attenuation-corrected PET data. **Results:** Visual inspection revealed a high degree of resemblance of generated pseudo-CT images compared to the acquired CT images in all validation data sets, with minor differences in individual anatomical details. Quantitative analyses revealed minimal underestimation below 5% of standardized uptake value (SUV) in all brain regions in independently attenuation-corrected PET data com-pared to the reference PET images. Color-coded error maps showed no regional bias and only minimal average errors around ±0%. Using independently attenuation-corrected PET data, no differences in image-based diagnoses were observed in 20 patients with neurological disorders compared to the reference PET images. **Conclusion:** Independent AC of brain $^{18}$F-FDG PET is feasible with high accuracy using the proposed, easy to implement deep learning framework. Further evaluation in clinical cohorts will be necessary to assess the clinical performance of this method.

*Hell J Nucl Med 2019; 22(3): 179-186* *Epub ahead of print: 7 October 2019* *Published online: 30 October 2019*

## Introduction

Positron emission tomography (PET) is a widely used medical imaging technique that offers unique insight into metabolic and functional processes in vivo. The distribution of a large number of available PET tracers can not only be detected non-invasively but can also be quantified, enabling a parametric and objective characterization of physiologic and pathologic processes. The technical prerequisite for accurate PET quantification is the reliable estimation of tissue attenuation for subsequent attenuation correction (AC). The gold standard for PET AC is given by transmission scanning using an external photon source [1]. However, with the introduction of integrated PET/computed tomography (PET/CT) scanners, this method was replaced by CT-based estimation of tissue attenuation which is now representing the clinical reference standard [2]. In the case of integrated PET/magnetic resonance imaging (PET/MRI), no direct measurement of tissue attenuation coefficients is possible and thus, AC has to be performed in an indirect way [3]. This challenge is being solved by relying on magnetic resonance imaging (MRI) data for tissue characterization and subsequent estimation of attenuation coefficients. To this end, several methods have been proposed, including segmentation-based AC, atlas-based AC and also machine learning-based methods [4-6].

Recently, a new class of specialized stand-alone PET scanners has been introduced with the purpose of specialized brain imaging-especially of neurodegenerative disorders-with a high spatial resolution at a low cost, potentially improving the availability of this imaging modality [7]. Clinical routine examinations, as well as clinical central nervous system (CNS) research, may significantly benefit from this technology. For these PET-only

scanners however, AC poses a challenge as they do not provide the capability of transmission scanning or additional CT/MR acquisition. So far, for these systems, AC can only be provided by a prior MR or CT scan of the region of interest in a separate scanner, and these data are subsequently imported and used for AC of the PET only scan. For many clinical indications, especially in CNS imaging, previous MR scans usually exist. This procedure, however, is associated with additional effort and cost and is prone to artifacts due to possible misalignment of image data.

An alternative for AC in standalone PET scanners would be direct AC using PET information only. In this context, the use of PET transmission data for estimation of attenuation maps has been proposed e.g. using time-of-flight information for combined PET reconstruction and AC [8]. As an alternative, the use of synthetic images for AC has been described before including atlas-based approaches [9-11].

Recently, potent machine learning methods for image translation have been introduced that may allow for a robust realization of this approach. Specifically Generative Adversarial Networks (GAN) have been shown to efficiently solve problems of image translation for numerous applications such as image reconstruction, image enhancement and translation between different modalities [12-16]. Generative Adversarial Networks are designed to tackle these tasks by using an adversarial structure where two convolutional neural networks (CNN) are trained simultaneously to perform opposing tasks. The Generator, resembling an au-toencoder, is trained to generate the target (e.g. perform image translation) whereas the Discriminator is trained to assess the performance of the Generator by classifying the translated output as real or fake in comparison to the ground truth sample. Using this approach, equilibrium is ideally reached where the Generator achieves optimal performance.

Generative Adversarial Networks have already been shown to achieve highly accurate results for related translation tasks such as MR-CT translation [17]. In our previous work, the feasibility of PET to CT translation was demonstrated from a methodological viewpoint using a deep learning approach named MedGAN [18]. This framework is optimized for the supervised translation of medical imaging data and was further assessed for other medical tasks such as the correction of motion artifacts in MR [19].

The purpose of this work was to adapt and evaluate the MedGAN framework for independent AC of brain fluorine-18-fluorodeoxyglucose ($^{18}$F-FDG) PET images only based on non attenuation corrected PET data ($PET_{NAC}$).

## Subjects and Methods

### Data

This study was approved by the Institutional Review Board of the University of Tübingen. Patient consent was waived by the institutional review board due to the retrospective and anonymized nature of data analysis. Fluorine-18-FDG PET/CT scans of the head region from 90 patients were acquired between 01/2017 and 10/2018 and retrospectively included in this study.

The 50 chronologically first $^{18}$F-FDG PET/CT data sets were used as training data (see below); these data were of patients that were examined in an oncological context. Another 20 data sets, also acquired in an oncological context with available PET sinogram raw data were used for the purpose of technical validation, hereby referred to as the technical validation dataset. In order to also assess the clinical performance of the proposed algorithm and its impact on diagnostic information, 20 patients that had been examined due to presence of suspected neurodegenerative or epileptic disorders with available PET sinogram data were used for clinical validation, referred to as the clinical validation dataset. Detailed patient information is summarized in Table 1.

***Table 1.*** *Patient characteristics.*

| | Training cohort (n=50) | Technical validation cohort (n=20) | Clinical validation cohort (n=20) |
|---|---|---|---|
| **Age [years]** | 60.6±16.6 | 61.2±16.4 | 62±19.1 |
| **Gender** | female 15, male 35 | female 7, male 13 | female 5, male 15 |
| **Weight [kg]** | 76.3±17.4 | 75.1±16.4 | 82.8±16.2 |
| **Height [m]** | 1.7±0.1 | 1.7±0.1 | 1.7±0.1 |
| **Diagnosis/ clinical question** | pharyngeal cancer (21) laryngeal cancer ( 5) thyroid cancer (13) cancer of unknown primary site (6) other (5) | pharyngeal cancer (10) laryngeal cancer(2) thyroid cancer (6) CUP (1) other (1) | dementia (12) epilepsy (6) other (2) |

All data sets were acquired on a state-of-the-art clinical PET/CT scanner (Biographm CT, Siemens Healthineers, Knoxville, Tennessee, U.S.A). Patients were positioned in a prone position with arms alongside the body. In order to minimize involuntary motion, patients were embedded in a vacuum mattress. In the 70 oncological patients, PET acquisition was performed 60 minutes after intravenous (i.v.)-injection of a body weight-adapted dose of 250-350MBq $^{18}$F-FDG. In the 20 neurological patients, PET was acquired 30 minutes after injection of 200-300MBq $^{18}$F-FDG.

In addition, a CT scan of the head was acquired for the purpose of attenuation correction. All PET data sets were reconstructed using the following parameters: matrix size 400 x 400; subsets 21; iterations 2, using a 2mm Gaussian filter without AC ($PET_{NAC}$) and for the validation data sets additionally using different CT-based and pseudo-CT-based attenuation maps for AC (see below).

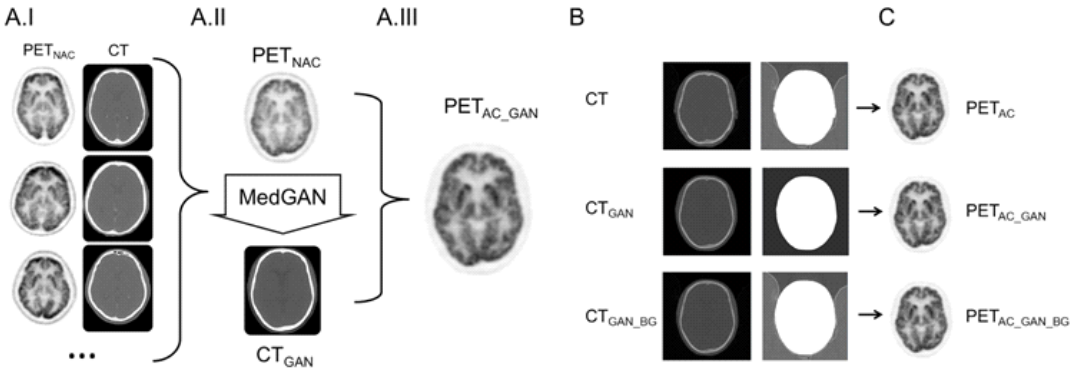


**Figure 1.** Generation of pseudo-CT for independent AC. **A.** Paired training data consisting (A.I) of non-attenuation corrected PET images ($PET_{NAC}$) and acquired CT data (CT) are used to train a GAN-based deep-learning framework (MedGAN). The trained generative network is then capable of creating pseudo-CT ($CT_{GAN}$) from previously unseen $PET_{NAC}$ images (A.II). These pseudo-CT can then be used for attenuation correction (A.III). **B.** Validation data sets were reconstructed using three CT data sets for AC: the originally acquired CT (CT), the pseudo-CT generated by the proposed framework ($CT_{GAN}$) and $CT_{GAN}$ with added background from the acquired CT ($CT_{GAN\_BG}$). The right column shows CT images in the lung window revealing the position mattress in the background (positioning mattress) of CT and $CT_{GAN-BG}$, which is not present in $CT_{GAN}$). **C.** Resulting PET data ($PET_{AC}$, $PET_{AC-GAN}$ and $PET_{AC-GAN-BG}$) after attenuation correction using the three CT data sets for AC. Visual qualitative inspection did not show any perceivable differences between the attenuation corrected PET data sets.

## Generation of pseudo-CT for independent AC

In order to achieve independent PET attenuation correction, a GAN-based deep-learning framework for the generation of pseudo-CT from non attenuation corrected PET images ($PET_{NAC}$) was implemented (Figure 1A) previously described in [18].

Typically, GAN consists of two neural networks trained together in competition, a convolutional Generator network G and a Discriminator network D. The Generator is tasked with generating realistic-looking synthetic data samples which attempt to fool the Discriminator. On the other hand, the Discriminator acts as a binary classifier by attempting to distinguish the generated synthetic data samples from the ground-truth data. In this work, to translate from input $PET_{NAC}$ images into corresponding pseudo CT images a variant of GAN, titled conditional GAN (cGAN), is utilized. In the case of the applied framework, the generator receives a $PET_{NAC}$ as input and translates it into a synthetic CT. The Discriminator then attempts to distinguish between the synthetic CT and the corresponding ground truth CT. Both networks are trained in competition via a min-max optimization task.

To enhance the global structure and details of the resultant CT images, the image translation task was carried out via the previously described MedGAN translation framework [18]. This framework consists of a cascaded U-net Generator architecture which receives $PET_{NAC}$ images as input. The Generator translates the input source domain images into corresponding synthetic CT images ($CT_{GAN}$) which are progressively refined via the subsequent encoder-decoder pairs with skip connections. In order for the Generator to capture the high and low frequency components of the desired ground truth CT scans, a combination of a Patch Discriminator architecture and a pre-trained feature extractor is used for loss calculations in addition to the adversarial loss (perceptual, style-reconstruction and content losses). These additional non-adversarial losses guide the Generator network to enhance the level of texture details and ensure the global homogeneity of the resultant CT images.

A paired dataset consisting of PETNAC and the corresponding CT data from 50 patients were used for training. Input and output images of the framework were independent 2D slices of the 3D data sets. The CT images of the training data were preprocessed by threshold-based cropping of background areas that do not contribute to the PET signal, including the surrounding positioning aid. The translation framework was trained on a single Nvidia 1080ti GPU for approximately 48hours, while the inference time for each translated CT image slice was found to be about 120 milliseconds. Validation was performed on 40 data sets (20 data sets for technical validation and 20 data sets for clinical validation).

## PET attenuation correction

For each of the 20 technical validation data sets, three PET reconstructions were carried out using the attenuation maps generated by: (i) the originally acquired CT (CT), (ii) the pseudo-CT created using MedGAN ($CT_{GAN}$) and (iii) a version of $CT_{GAN}$ in which the extracorporeal background from CT was added to $CT_{GAN}$ in order to account for attenuation caused by the surrounding vacuum mattress ($CT_{GAN-BG}$) (Figure 1B). This background CT-information was not included in the training procedure as background areas not contributing to the PET signal were cropped in the CT training data. By generating $CT_{GAN-BG}$ we aimed to correct for errors caused by background attenuation in contrast to errors caused by the pseudo-CT-based AC as such.

Using these CT and pseudo-CT data for AC, $^{18}$F-FDG PET images were reconstructed and attenuation-corrected using a 3D ordered subset expectation maximization algorithm (3D OSEM) provided by the vendor as described above

All 20 technical validation data sets thus produced the attenuation-corrected datasets: (i) $PET_{AC}$ using the original CT, (ii) $PET_{AC-GAN}$ using the $CT_{GAN}$ and (iii) $PET_{AC-GAN-BG}$ using $CT_{GAN-BG}$ (Figure 1B). For the 20 clinical validation data sets, $PET_{AC}$ and $PET_{AC-GAN-BG}$ were reconstructed in the same way.

## Data analysis

### Qualitative analysis

For qualitative evaluation, the pseudo-CT images ($CT_{GAN}$ and $CT_{GAN-BG}$) as well as the attenuation corrected PET ima-ges ($PET_{AC-GAN}$ and $PET_{AC-GAN-BG}$) generated on the validation data set were inspected by a Radiologist (S.G.) with 8 years of experience in Radiology and 6 years of experience in hy-brid imaging and compared to the reference data (CT and $PET_{AC}$). The occurrence of artifacts was recorded. In addition, differences in the depiction of the following predefined anatomical landmarks between CT and $CT_{GAN}$ were recorded: skull shape, skull thickness, size of the paranasal sinuses and mastoid cells, size of the nasal cavity, location of ventricles.

### Quantitative analysis

In order to ensure objective and reproducible quantitative analysis, all attenuation corrected PET data sets generated on the 40 validation data sets were non-rigidly spatially normalized to MNI space using SPM 8 and the herein provided standard template [20,21]. This allowed for automated segmentation of brain regions and comparison of PET standardized uptake values (SUV) as well as generation of difference, percent difference and absolute percent difference maps of $PET_{AC-GAN}$ and $PET_{AC-GAN-BG}$ compared to the reference $PET_{AC}$.

In detail, after normalization to MNI space, mean SUV of the frontal, parietal, occipital, temporal, insular and cerebellar cortex as well as the putamen were automatically extracted from all attenuation-corrected PET data sets using volumes of interest provided by the AAL (automated anatomical labeling) labels and an in-house Matlab script (Matlab Version 2014b, Mathworks, Nattick, USA) [22].

Differences and percent differences of measured SUV of $PET_{AC-GAN}$ and $PET_{AC-GAN-BG}$ compared to $PET_{AC}$ were calculated as $PET_{AC-GAN}$-$PET_{AC}$, $100\cdot(PET_{AC-GAN}-PET_{AC})/PET_{AC}$ and $PET_{AC-GAN-BG}$-$PET_{AC}$, $100\cdot(PET_{AC-GAN-BG}-PET_{AC})/PET_{AC}$ respectively. Absolute percent differences were computed as $100\cdot|PET_{AC-GAN}-PET_{AC}|/PET_{AC}$ and $100\cdot|PET_{AC-GAN-BG}-PET_{AC}|/PET_{AC}$.

Positron emission tomography quantification errors are presented as box plots depicting the mean (circle), median (line), standard deviation (box) and minimum and maximum values (whiskers).

For the purpose of visual depiction of differences in SUV quantification in $PET_{AC-GAN}$ and $PET_{AC-GAN-BG}$ compared to $PET_{AC}$, color-coded population-averaged difference, percent difference and absolute percent difference maps averaged over the technical validation data set were generated using the normalized attenuation-corrected PET data.

### Clinical evaluation

In order to assess the impact of the proposed framework with respect to imaging-based diagnosis, all 20 clinical validation data sets were analyzed by a Nuclear Medicine physician with over 20 years of experience in CNS PET imaging (MR). Image-based diagnoses were established by visual assessment as well as statistical analysis of brain metabolism and subsequent visualization using stereotactic surface projections (SSP) (Neurostat, Neuroimaging and Biotechnology Laboratory, University of Utah, [23]) of $PET_{AC}$ and $PET_{AC-GAN-BG}$ in comparison.

## Results

### Qualitative analysis

Qualitative analysis of generated pseudo-CT ($CT_{GAN}$) data revealed a high level of realism with detailed and realistic depiction of anatomical structures of the head for both the technical and clinical validation data sets (Figure 2A,B). Due to the 2D slice-per-slice generation of pseudo-CT images, blurring and slight between-slice inconsistencies were observed especially of the skull in cranial parts (Figure 2A). When comparing $CT_{GAN}$ to the acquired CT data, we observed slight differences in individual anatomical details (Figure 2B). Specifically, the size and shape of air-filled spaces (paranasal sinus and mastoid cells) were appreciably different in $CT_{GAN}$ compared to the acquired CT in 23 of 40 patients, especially in patients with prominent frontal sinuses. Furthermore, slight differences in the estimated skull thickness were observed in 9 of 40 patients especially in the frontal and occipital bone region. In one patient with enlarged lateral ventricles, an artifact was observed within the lateral ventricle in the form of erroneously generated bone tissue (Figure 2C). In the remaining validation data sets, no relevant difference in skull shape and position of ventricles was observed between CT and $CT_{GAN}$. No appreciable distortions or were observed. Visual comparison of the resulting PET images did not reveal any appreciable differences between $PET_{AC}$ and $PET_{AC-GAN}$ or $PET_{AC-GAN-BG}$ (Figure 2B).

### Quantitative analysis

Quantitative analysis revealed slight underestimation of SUV in $PET_{AC-GAN}$ compared to $PET_{AC}$. In the technical validation data set, the population-averaged mean percent difference in SUV between $PET_{AC}$ and $PET_{AC-GAN}$ over all the predefined brain regions amounted to -6.2%. The highest population-averaged percent SUV underestimation in $PET_{AC-GAN}$ was observed in the parietal cortex (-7.8%); the lowest error was observed in the occipital cortex (-4.5%).Absolute percent difference between $PET_{AC}$ was on average at 6.3% (Figure 3A).

When accounting for background attenuation, the quantification error was markedly decreased in $PET_{AC-GAN-BG}$ to a population-averaged percent difference between $PET_{AC}$ and $PET_{AC-GAN-BG}$ of -1.5%. The highest population-averaged percent error in $PET_{AC-GAN-BG}$ was observed in the frontal cortex (-2.5%); the lowest error was observed in the occipital cortex (+0.6%).The absolute percent difference was reduced

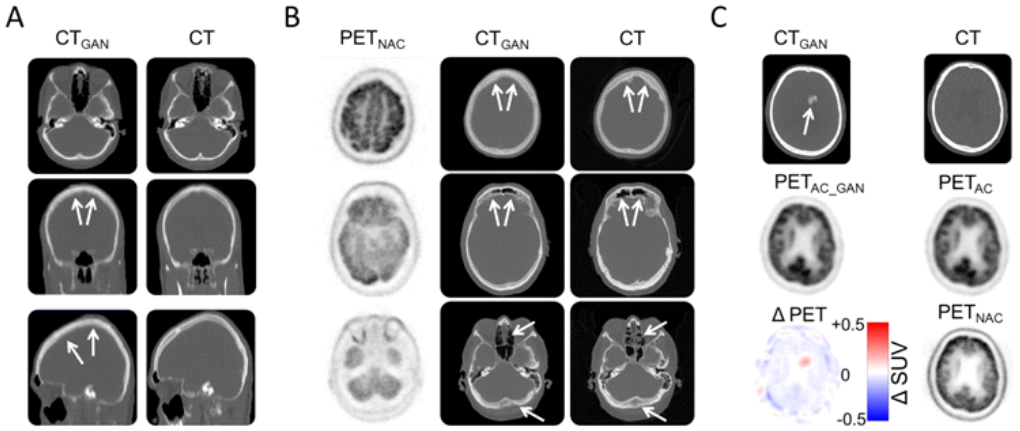


**Figure 2.** Results of $PET_{NAC}$ to CT translation. **A.** Example of a generated pseudo-CT ($CT_{GAN}$, left column) compared to the acquired reference CT (CT, right column). In coronal (middle row) and sagittal (bottom row) views, blurring and slight inconsistencies of the skull can be observed in areas of flat orientation of the skull (arrows) caused by the 2D slice-per-slice generation of the pseudo-CT by the proposed framework. **B.** Examples of generated pseudo-CT images ($CT_{GAN}$, middle column) of three patients at different anatomical levels compared to the corresponding acquired CT images (CT, right column). Input $PET_{NAC}$ images are shown in the left column. The generated $CT_{GAN}$ showed a high level of realism without appreciable artifacts. The arrows point to regions of slight differences between $CT_{GAN}$ and CT concerning individual anatomical details mainly located in the area of paranasal sinuses (middle and bottom example) or frontal and occipital bone structures of the skull (top and bottom examples). **C.** Artifact observed in a single patient with relatively wide lateral ventricles. The pseudo-CT ($CT_{GAN}$, left upper part) displays an area of falsely identified bone within the anterior part of the left lateral ventricle (arrow). This resulted in a slight local overestimation in the corresponding PET ($PET_{AC\text{-}GAN}$, left middle part) compared to the original PET ($PET_{AC}$, right middle part; SUV difference map Δ PET=$PET_{AC\text{-}GAN}$-$PET_{AC}$, left lower part). The non-attenuation corrected PET ($PET_{NAC}$) is shown in the right lower part.

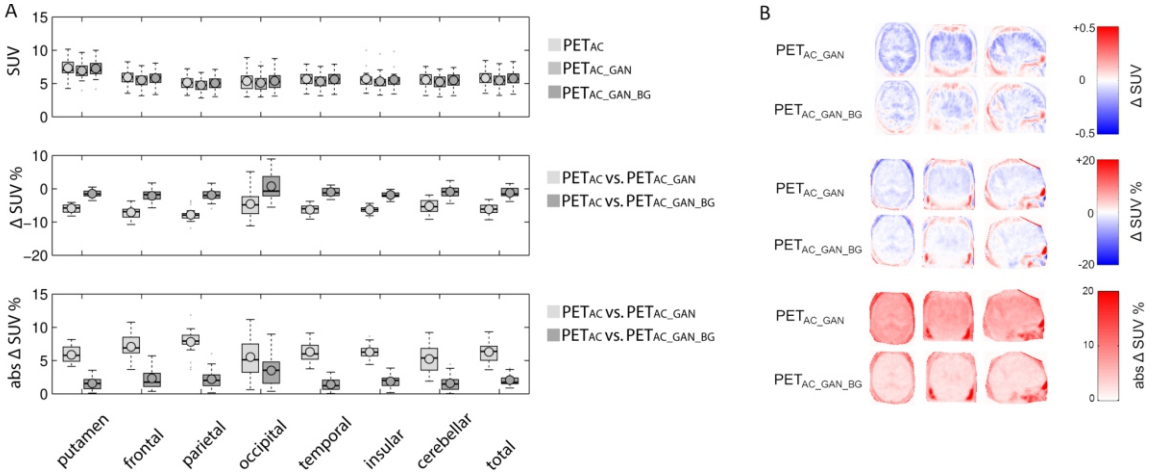


**Figure 3.** Quantitative results of technical validation. **A.** Mean SUV of $PET_{AC}$, $PET_{AC\text{-}GAN}$ and $PET_{AC\text{-}GAN\text{-}BG}$ of the 20 technical validation data sets in analyzed brain regions (upper part). While $PET_{AC\text{-}GAN}$ showed a slight underestimation of SUV compared to $PET_{AC}$ of -6.2% on average, correcting for background attenuation decreased the observed averaged error to -1.5% $PET_{AC\text{-}GAN\text{-}BG}$ (middle part). Similarly, the absolute percent deviation of $PET_{AC\text{-}GAN\text{-}BG}$ compared to $PET_{AC}$ was below 5% in average (lower part). **B.** Population-averaged SUV difference (upper part), relative percent SUV difference (middle part) and absolute percent SUV differences of $PET_{AC\text{-}GAN}$ and $PET_{AC\text{-}GAN\text{-}BG}$ compared to $PET_{AC}$. $PET_{AC\text{-}GAN}$ shows a slight homogeneous relative underestimation of SUVs within the brain region without larger regional bias. This error is reduced to values around ±0 in average in $PET_{AC\text{-}GAN\text{-}BG}$. Higher relative errors can be observed in surrounding areas of the skull and especially in the region of air-filled cavities (e.g. frontal sinus and mastoid cells).

on average to 2.1% in $PET_{AC\text{-}GAN\text{-}BG}$ (Figure 3A). Similar quantitative results were observed in the clinical validation data set (Figure 4A).

Color-coded population-averaged error maps of the difference, percent difference and absolute percent difference of the technical validation data set of $PET_{AC\text{-}GAN}$ and $PET_{AC\text{-}GAN\text{-}BG}$ compared to $PET_{AC}$ confirmed these quantitative results (Figure 3B). These error maps showed a homogeneous distribution of the percent error and absolute percent error over all the brain regions with $PET_{AC\text{-}GAN\text{-}BG}$ showing only minimal deviations from $PET_{AC}$ around ±0% on average. In the surrounding tissue, especially within the skull and in the region of paranasal sinuses and mastoid cells, we observed a quantification error of $PET_{AC\text{-}GAN}$ and $PET_{AC\text{-}GAN\text{-}BG}$ compared to $PET_{AC}$ of more than -10% to -20% in average (Figure 3B).

## Clinical evaluation

Clinical analysis of the 20 clinical validation data sets including assessment of SSP revealed no difference in diagnostic image information between $PET_{AC}$ and $PET_{AC\text{-}GAN\text{-}BG}$ (Figure 4B). Taking into account the initial clinical question (dementia n=12, epilepsy n=6, other n=2) no pathologic brain glu-

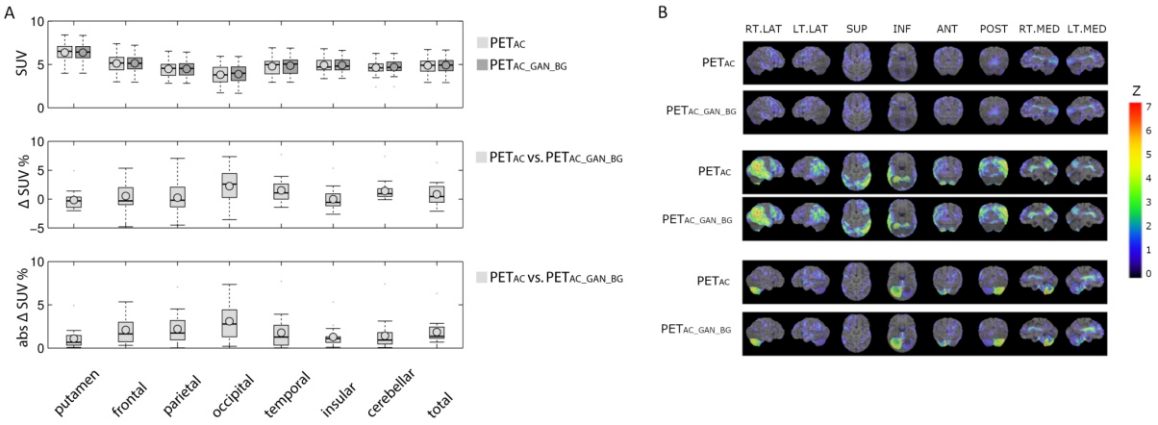


**Figure 4.** Quantitative results of clinical validation. **A.** Mean SUV of $PET_{AC}$ and $PET_{AC\text{-}GAN\text{-}BG}$ of the 20 clinical validation data sets in analyzed brain regions (upper part). Percent error (middle part) and absolute percent error (lower part) of $PET_{AC\text{-}GAN\text{-}BG}$ compared to $PET_{AC}$ was below 5% on average. **B.** Stereotactic surface projections of $PET_{AC}$ and $PET_{AC\text{-}GAN\text{-}BG}$ of 3 patients from the clinical validation data sets. Upper part: 42 y/o female patient with repeated seizures. PET revealed no pathologic metabolism in $PET_{AC}$ or $PET_{AC\text{-}GAN\text{-}BG}$. Middle part: 71 y/o patient with posterior cortical atrophy. Fluorine-18-FDG-PET shows occipital, parietal and temporal hypometabolism in $PET_{AC}$ and $PET_{AC\text{-}GAN\text{-}BG}$. Lower part: Patient with cerebellar ataxia. Fluorine-18-FDG-PET reveals significant hypometabolism of the right cerebellum in $PET_{AC}$ and $PET_{AC\text{-}GAN\text{-}BG}$.

cose metabolism was observed in 9 of 20 patients. In 6 patients, Parkinson-associated dementia was diagnosed. An epileptogenic focus (n=2), posterior cortical atrophy (n=2) and acute encephalitis (n=1) were diagnosed in the remaining patients.

## Discussion

In this study, we introduced and evaluated a GAN-based deep learning method for brain $^{18}$F-FDG PET AC using only PET data. Using this proposed framework, we observed accurate results in PET quantification compared to the clinical reference standard of CT-based AC with quantification errors well below 5% on average after accounting for background attenuation caused by the positioning aid. This demonstrates very high quantitative precision of pseudo-CT-based AC. Furthermore, we did not observe bias concerning the distribution of quantification errors throughout the brain.

Our results show a measurable effect of the patient positioning mattress on PET quantification that is higher than the minimal error caused by pseudo-CT-based AC. Thus, it is important to account for this error when using pseudo-CT based AC in a clinical setting. This can be solved by using standardized background materials with known position and attenuation coefficients as is routinely done in integrated PET/MRI [24, 25]. Direct estimation of background material within the proposed deep learning framework is not feasible as it does not contribute to the PET signal and is thus invisible in $PET_{NAC}$.

Based on these results, the proposed approach for independent PET attenuation correction can be used in PET-only brain PET scanners avoiding additional CT or MR scans for PET AC and thus reducing examination time and unnecessary radiation exposure by CT. In addition, this method may also be of interest for AC in combined PET/CT or PET/MR in case of artifact-corrupted CT or MR image data due to motion, misalignment, metal artifacts or erroneous tissue segmentation [26]. In these cases, AC based only on PET may provide higher robustness [27]. Similar approaches for MR-based PET attenuation correction were recently proposed that use deep learning for estimation of attenuation coefficients from MR data [4, 28]. The authors reported similarly low quantification errors.

The novelty of this work lies in the use of a GAN for medical image translation and specifically independent PET attenuation correction. Concurrent to our work on MedGAN, other approaches have been proposed for generating pseudo-CT images for independent PET AC. Most similar to our approach, the deep AC framework utilized an autoencoder-based architecture or voxel-wise classification to generate CT from input NACPET images [29]. From a methodological perspective, the adversarial training procedure used in our work has been shown to result in superior performance in comparison to traditional autoencoder-based approaches for a variety of translational and super-resolution tasks. This also can be assessed qualitatively, where the generated pseudo-CT by MedGAN exhibit distinctive improvement to textural details and overall realism [18]. This is attributed to both the adversarial training procedure as well as the feature-based non-adversarial losses utilized by MedGAN to ensure global and textural consistency of the output CT images. Furthermore, we were able to demonstrate the clinical applicability of deep learning-based independent PET AC in addition to its technical feasibility.

Computed tomography-independent PET AC has been proposed and validated before using atlas-based approaches for PET only as well as PET/MR [5,10,11,30,31]. In contrast to atlas-based methods, translation-based generation of pseudo-CT images is independent of deformable registration models used in atlas-based AC. Thus, GAN-based methods can be expected to provide more realistic and robust pseudo-CT data for a wide range of anatomical variability, if a representative training data set is available. In our study, we observed artifacts using the proposed method in

patients with anatomical particularities that were not sufficiently represented in the training set. In order to cover these cases, a larger representative training data base will be helpful. The relatively small training dataset of our study (n= 50 3D data sets) already led to satisfactory qualitative and quantitative results due to the paired training setup, redundant information between neighboring slices and the relatively constant anatomy of the skull and brain. A similar range of necessary training data was reported in previous studies [4,14,16].

Independent of the specific generation method, the use of synthetic images for AC has principle advantages and disadvantages compared to the use of previously acquired and registered image data. Synthetic attenuation correction may simplify the workflow, potentially reduce cost and does not require image registration. The use of previously acquired images for AC has the advantage of depicting the individual anatomical configuration of the single patient which can be especially important in cases of atypical anatomy, e.g. after major surgery. On the other hand, the previous acquisition of MR or CT images for PET AC may introduce other sources of artifacts e.g. metal artifacts or motion artifacts that may influence PET quantification. Thus, the capability of using either way of PET AC should be accessible on the respective scanners and the choice of method should be based on the clinical question and patient characteristics.

The proposed method is not limited to PET AC and can be extended to AC of SPET data when a CT is not available. This is of practical relevance as AC of SPET data has been shown to potentially improve diagnostic confidence for a number of indications, especially for myocardial SPET [32-35].

The described approach has the limitation of 2D slice-per-slice generation of pseudo-CT images resulting in minor inconsistencies between neighboring slices. A 3D approach can be expected to provide a higher level of accuracy of the generated pseudo-CT and reduce artifacts by exploiting image information in the third dimension. However, 3D translation using GAN is a computationally expensive task and remains to be optimized in future projects.

We performed a methodological study demonstrating the technical feasibility and accuracy of the method in a relatively small patient cohort. The performance of the proposed method in a wider clinical context has to be assessed in clinical studies and larger patient populations. Furthermore, the applicability to non-$^{18}$F-FDG tracers remains to be established for this method to reach the state of clinical applicability.

*In conclusion*, independent attenuation correction of brain $^{18}$F-FDG PET is feasible with high accuracy using the proposed, easy to implement deep learning framework. Further evaluation in clinical cohorts will be necessary to assess the clinical performance of this method.

*The authors declare that they have no conflicts of interest*

## Bibliography


1. Bailey DL. Transmission scanning in emission tomography. *Eur J Nucl Med* 1998; 25: 774-87.
2. Kinahan PE, Townsend DW, Beyer T et al. Attenuation correction for a combined 3D PET/CT scanner. *Med Phys* 1998; 25: 2046-53.
3. Vandenberghe S, Marsden PK. PET-MRI: a review of challenges and solutions in the development of integrated multimodality imaging. *Phys Med Biol* 2015; 60: R115-54.
4. Liu F, Jang H, Kijowski R et al. Deep Learning MR Imaging-based Attenuation Correction for PET/MR Imaging. *Radiology* 2018; 286: 676-84.
5. Bezrukov I, Mantlik F, Schmidt H et al. MR-Based PET attenuation correction for PET/MR imaging. *Semin Nucl Med* 2013; 43: 45-59.
6. Chen Y, An H. Attenuation Correction of PET/MR Imaging. *Magn Reson Imaging Clin N Am* 2017; 25: 245-55.
7. Watanabe M, Saito A, Isobe T et al. Performance evaluation of a high-resolution brain PET scanner using four-layer MPPC DOI detectors. *Phys Med Biol* 2017; 62: 7148-66.
8. Berker Y, Li Y. Attenuation correction in emission tomography using the emission data-A review. *Med Phys* 2016; 43: 807-32.
9. Merida I, Reilhac A, Redoute J et al. Multi-atlas attenuation correction supports full quantification of static and dynamic brain PET data in PET-MR. *Phys Med Biol* 2017; 62: 2834-58.
10. Sjolund J, Forsberg D, Andersson M et al. Generating patient specific pseudo-CT of the head from MR using atlas-based regression. *Phys Med Biol* 2015; 60: 825-39.
11. Burgos N, Cardoso MJ, Thielemans K et al. Attenuation correction synthesis for hybrid PET-MR scanners: application to brain studies. *IEEE Trans Med Imaging* 2014; 33: 2332-41.
12. Goodfellow IJ, Pouget-Abadie J, Mirza M et al. Generative Adversarial Networks. *ArXiv e-prints*; 2014.
13. Isola P, Zhu J-Y, Zhou T et al. Image-to-Image Translation with Conditional Adversarial Networks. *ArXiv e-prints*; 2016.
14. Wang Y, Yu B, Wang L et al. 3D conditional generative adversarial networks for high-quality PET image estimation at low dose. *Neuroimage* 2018; 174: 550-62.
15. Choi H, Lee DS. Generation of Structural MR Images from Amyloid PET: Application to MR-Less Quantification. *J Nucl Med* 2018; 59: 1111-7.
16. Chartsias A, Joyce T, Dharmakumar R et al. Adversarial Image Synthesis for Unpaired Multi-modal Cardiac Data, 2017; Cham.
17. Wolterink JM, Dinkla AM, Savenije MHF et al. Deep MR to CT Synthesis using Unpaired Data. *ArXiv e-prints*; 2017.
18. Armanious K, Yang C, Fischer M et al. MedGAN: Medical Image Translation using GANs. *ArXiv e-prints*; 2018.
19. Kustner T, Armanious K, Yang J et al. Retrospective correction of motion-affected MR images using deep learning frameworks. *Magn Reson Med* 2019; 82(4):1527-40.
20. Ashburner J. SPM: a history. *Neuroimage* 2012; 62: 791-800.
21. Evans AC, Janke AL, Collins DL et al. Brain templates and atlases. *Neuroimage* 2012; 62: 911-22.
22. Tzourio-Mazoyer N, Landeau B, Papathanassiou D et al. Automated anatomical labeling of activations in SPM using a macroscopic anatomical parcellation of the MNI MRI single-subject brain. *Neuroimage* 2002; 15: 273-89.
23. Minoshima S, Frey KA, Koeppe RA et al. A diagnostic approach in Alzheimer's disease using three-dimensional stereotactic surface projections of fluorine-18-FDG PET. *J Nucl Med* 1995; 36: 1238-48.
24. Eldib M, Bini J, Faul DD et al. Attenuation Correction for Magnetic Resonance Coils in Combined PET/MR Imaging: A Review. *PET Clin* 2016; 11: 151-60.
25. Oehmigen M, Lindemann ME, Lanz T et al. Integrated PET/MR breast cancer imaging: Attenuation correction and implementation of a 16-channel RF coil. *Med Phys* 2016; 43: 4808.
26. Kong E, Cho I. Clinical issues regarding misclassification by Dixon based PET/MR attenuation correction. *Hell J Nucl Med* 2015; 18(1): 42-7.
27. Buchbender C, Hartung-Knemeyer V, Forsting M et al. Positron emission tomography (PET) attenuation correction artefacts in PET/CT and PET/MRI. *Br J Radiol* 2013; 86: 20120570.
28. Gong K, Yang J, Kim K et al. Attenuation correction for brain PET imaging using deep neural network based on Dixon and ZTE MR images. *Phys Med Biol* 2018; 63: 125011.

29. Liu F, Jang H, Kijowski R et al. A deep learning approach for $^{18}$F-FDG PET attenuation correction. *EJNMMI Phys* 2018; 5: 24.
30. Dewan M, Zhan Y, Hermosillo G et al. Brain PET Attenuation Correction without CT: An Investigation. Paper presented at: 2013 International Workshop on Pattern Recognition in Neuroimaging; 22-24 June 2013, 2013.
31. Rausch I, Rischka L, Ladefoged CN et al. PET/MRI for Oncologic Brain Imaging: A Comparison of Standard MR-Based Attenuation Corrections with a Model-Based Approach for the Siemens mMR PET/MR System. *J Nucl Med* 2017; 58:1519-25.
32. Xin WC, Shao XL, Wang YT et al. Is there an incremental value to use myocardial perfusion imaging with or without CT attenuation for the diagnosis of coronary artery disease? A study in Chinese patients. *Hell J Nucl Med* 2018; 21(1): 48-54.
33. Apostolopoulos DJ, Savvopoulos C. What is the benefit of CT-based attenuation correction in myocardial perfusion SPET? *Hell J Nucl Med* 2016; 19(1): 89-92.
34. Shawgi M, Tonge CM, Lawson RS et al. Attenuation correction of myocardial perfusion SPET in patients of normal body mass index. *Hell J Nucl Med* 2012;15(3): 215-9.
35. Kalantari F, Rajabi H, Saghar M. Quantification and reduction of attenuation related artifacts in SPET by applying attenuation model during iterative image reconstruction: a Monte Carlo study. *Hell J Nucl Med* 2011; 14(3): 278-83.


*Ramon Casas (1866-1932). Sífilis, 1900. Poster 80x34cm. Museu Nacional d'Art de Catalunya. Spain.*